Chemical Engineering Journal 452 (2023) 139223

Contents lists available at ScienceDirect

Chemical Engineering Journal

journal homepage: www.elsevier.com/locate/cej

Conducting polymer host–guest hydrogels with bicontinuous electron/ion transport for boosted thickness–independent supercapacitance

Le Li [a], Yufeng Wang [b], Xuran Bao [a], Dai Hai Nguyen [c], Chao Zhang [b,*], Tianxi Liu [a,b,*]

[a] Key Laboratory of Synthetic and Biological Colloids, Ministry of Education, School of Chemical and Material Engineering, International Joint Research Laboratory for Nano Energy Composites, Jiangnan University, Wuxi 214122, PR China
[b] State Key Laboratory for Modification of Chemical Fibers and Polymer Materials, College of Materials Science and Engineering, Donghua University, Shanghai 201620, PR China
[c] Institute of Applied Materials Science, Vietnam Academy of Science and Technology, Ho Chi Minh City, Vietnam

ARTICLE INFO

Keywords:
Polypyrrole-based aerogel
Elasticity
Self-healing
Bicontinuous conductive structure
Thickness-independent electrode

ABSTRACT

The development of conducting polymer hydrogels with 3D ordering and hierarchical geometry is urgent yet challenging for the design of electrochemical/electronic systems with combined features of hydrogel structures and pseudocapacitive organic materials. Herein, a host–guest hybrid gel electrode that is composed of a polypyrrole (PPy) aerogel and its skeleton-surface-constrained Fe^{3+}-coordinated poly(acrylic acid) (Fe-PAA) hydrogel is fabricated, which can readily work as a highly elastic and self-healable electrode for an all-gel-state supercapacitor with thickness-independent capacitive performance. An interfacial polymerization approach by restraining oxidative nucleation and promoting secondary growth reactions is presented for preparing the pseudocapacitive PPy aerogel as a host component with good elasticity. Upon an impregnation with the ionically conductive and self-healable Fe-PAA hydrogel as a guest component, the resultant PPy aerogel-hosting hydrogels (PAHH) exhibit a remarkable thickness-independent supercapacitance owing to the enhanced electron/ion transport kinetics induced by a bicontinuous electron/ion-conducting network. A proof-of-concept all-solid-state supercapacitor based on the host–guest hybrid electrodes demonstrates a remarkable remarkably high areal capacitance of 2033 mF cm^{-2} and extremely steady retention undergoing a 60 % compression deformation and cutting damage with high self-healing performance. The host–guest geometry design for the development of bicontinuous electron/ion conductive transport in conducting polymer-based electrodes might boost unprecedented electron and ion transport in high-mass-loading thick electrodes for smart energy storage devices.

1. Introduction

Exploration of energy storage devices that can undergo complex deformations of bending, stretching and compressing is the focus of upcoming energy systems and is urgently demanded in wearable electronics [1–6]. Flexible supercapacitors are regarded as promising wearable energy storage devices among numerous energy storage devices featured with easy fabrication, fast delivery rate and durable life [7–11]. Flexible supercapacitors undergoing large deformations without sacrificing their electrochemical performances are highly demanded [12–15]. To date, substantial efforts have been devoted to fabricating flexible supercapacitors with intrinsic and structural flexibility for wearable electronics [16–20]. Among these, conducting polymer-based hydrogels feature the combination of large intrinsic conductivity derived from conducting polymers and high-deformation tolerance derived from hydrogels, which are therefore considered ideal electrodes for flexible supercapacitors [12,18,21–24]. Various approaches have been devoted-applied to constructing electrodes made from conducting polymer-based hydrogels with enhanced energy storage performances that could be classified into two categories. First, conducting polymer-based hydrogels are prepared by directly cross-linking conducting polymers with dopant molecules by in-situ polymerization [25,26]. The resulting conducting polymer-based hydrogels usually process outstanding conductivity and electrochemical performances owing to the formation of 3D continuous phases of conducting polymers. However, this kind of conducting polymer-based hydrogels usually exhibits

* Corresponding authors at: Key Laboratory of Synthetic and Biological Colloids, Ministry of Education, School of Chemical and Material Engineering, International Joint Research Laboratory for Nano Energy Composites, Jiangnan University, Wuxi, 214122, PR China (T. Liu); State Key Laboratory for Modification of Chemical Fibers and Polymer Materials, College of Materials Science and Engineering, Donghua University, Shanghai 201620, PR China (C. Zhang).
E-mail addresses: czhang@dhu.edu.cn (C. Zhang), txliu@jiangnan.edu.cn (T. Liu).

https://doi.org/10.1016/j.cej.2022.139223
Received 8 July 2022; Received in revised form 23 August 2022; Accepted 11 September 2022
Available online 16 September 2022

easy embrittlement and poor structural stability under deformations and long-term cycles. Second, conducting polymer-based hydrogels are prepared by in-situ polymerization of conducting polymers within the network of pre-designed elastic hydrogels [1,27,28]. This approach presents a simple fabrication method for constructing versatile conducting polymer-based hydrogels with desired elasticity and structural stability via choosing suitable elastic hydrogel substrates. However, mass loadings of electrochemically active conducting polymers in hydrogels are relatively low (typically less than 10 mg cm^{-2}), ascribed to the poor swelling and sluggish diffusion of monomers within the existed hydrogel matrix [29–32]. Thus, the development of conducting polymer-based hydrogels with desired elasticity and electrochemical performance is highly demanded yet still challenging.

Fabrication of thick electrodes with high loading of active materials is appealing in supercapacitor applications as they could efficiently reduce the fractions of inactive device components like current collectors and separators, thereby enabling the resultant devices with the feature of lightweight and high energy density [33–37]. Unfortunately, the simple increase in thickness of traditional electrode materials leading to largely restricted electrochemical performances due to thick electrodes would cause structural brittleness and poor cycling stability [34,38]. Furthermore, the increased thickness of electrodes would result in sluggish ion/electron transport kinetics [22,38]. Therefore, it is urgent to establish high-loading thick electrodes from conducting polymer-based hydrogels with simultaneously enhanced electrochemical energy storage and compression-tolerant performance.

Herein, unique polypyrrole (PPy) aerogel-hosting hydrogels with bicontinuous electron/ion transport are creatively developed by skeleton-surface-confined polymerization of Fe^{3+}–coordinated poly (acrylic acid) (Fe-PAA) hydrogels within the performed 3D-interconnected PPy aerogels as host. The Fe-PAA hydrogels with reversible association/dissociation of hydrogen bonds and coordinations contribute to efficient energy dissipation upon deformation, endowing the host–guest PPy hydrogel electrodes with impressive superelasticity and fast self-healing property. The PPy aerogel-hosting hydrogels feature bicontinuous conductive structures of electrically conductive PPy aerogels and ionically conductive Fe-PAA hydrogels. As a result, thick electrodes of the elaborated PPy aerogel–hosting hydrogels simultaneously combine features of superelasticity, interpenetrating conducting network and intrinsic self-healability, thereby endowing the resultant all-solid-state supercapacitors with high-mass-loading electrochemical active material, enhanced electrode/electrolyte interface, promising electrochemical performance and unique damage–tolerance capability. The host–guest geometry design for the development of bicontinuous conductive networks in conducting polymer-based electrodes might helps overcome the charge-transport challenges in fabrications of high-mass-loading thick electrodes for smart energy storage devices.

2. Materials and methods

2.1. Materials

Acrylic acid (AA, AR, ≥ 98 %), ethanol (AR, ≥ 99.7 %), ammonium persulfate (APS, AR, ≥ 98 %), KNO_3 (AR, ≥ 99.5 %) and $Fe(NO_3)_3{\cdot}9H_2O$ (AR, ≥ 98.5 %) were purchased from Sinopharm Chemicals. Pyrrole was obtained from Sigma-Aldrich and distilled before use. Deionized (DI) water was used throughout the experiments.

2.2. Preparation of the PPy aerogels

3D PPy aerogels were one-pot synthesized by interfacial polymerization. Typically, 10 mmol of pyrrole was dissolved in 4.7 mL of isopropyl alcohol at 0 °C, and 10 mmol of $Fe(NO_3)_3{\cdot}9H_2O$ was dissolved in 4.7 mL of water at 0 °C. After being mixed rapidly under agitation for 10 s, the mixed solution was injected into a plastic mold for polymerization at 0 °C for 1 h, and then placed at 25 °C without stirring for a designed amount of time to form PPy hydrogels. The prepared PPy hydrogels were soaked in ethanol and water in sequence to remove unreacted monomers and impurities, and freeze-dried to obtain PPy aerogels. The PPy1, PPy2, PPy3 and PPy4 represent the PPy aerogel samples prepared by interfacial polymerization for 1, 24, 120 and 240 h, respectively.

2.3. Preparation of the PAHH

PPy aerogel-hosting hydrogel was prepared by in-situ polymerization of Fe^{3+}-crosslinked PAA (Fe-PAA) hydrogels confined on the skeleton surface of the prepared PPy aerogels. PPy aerogels were infiltrated in a vacuum and swelled with an aqueous solution containing the AA (1 mL), APS (5 mg), $LiNO_3$ (5 mmol), $Fe(NO_3)_3{\cdot}9H_2O$ (0.1 mmol) and water (4 mL). After being degassed with nitrogen and heated at 70 °C for 24 h, the PAHH was then obtained. A comparison sample of neat Fe-PAA hydrogel was prepared without using the PPy aerogels while keeping other conditions similar to the preparation method for the PAHH.

2.4. Assembly of the ASC devices

The ASC devices using the prepared PAHH as electrodes were assembled by sandwiching two pieces of PAHH electrodes (2 × 1 × 0.1 cm^3) with one Fe-PAA hydrogel electrolyte (2.2 × 1.2 × 0.1 cm^3) under a pressure of 20 kPa for 3 min. The total contact areas of electrodes in the device were measured as 2.0 cm^2. Thicknesses of PAHH electrodes were regulated to satisfy the devices with various mass loadings of PPy. The as-fabricated ASC devices were sealed with polyester films to ensure long-term testing. The control device denoted as PPy-based ASC was assembled by using neat PPy aerogels instead of PAHH as the electrode while keeping other fabrication conditions similar to the fabrication of PAHH-based devices. The capacitance recovery of PAHH was measured after 2-hour self-healing at room temperature.

3. Results and discussion

Fig. 1a demonstrates the structural design and synthetic procedure of host–guest PPy aerogel-hosting hydrogels (PAHH). Highly 3D-interconnected PPy aerogels were first prepared by interfacial polymerization of pyrrole (monomer) in a mixed solvent of water and isopropyl alcohol with water-soluble ferric nitrate as an oxidizing agent (initiator). Pyrrole monomers and oxidizing agents were initially enriched in water and isopropyl alcohol, respectively. Polymerization of pyrrole occurred at the vigorously-stirred interface followed by a long-term reaction without stirring, thus forming a PPy framework with unique 3D structures. Through subsequent in-situ polymerization by using the PPy aerogels as a host, Fe-PAA hydrogels were generated and constrained to the skeleton surface of PPy aerogels. 3D nanostructured PPy aerogels and ion-rich Fe-PAA hydrogels are integrated into PAHH with bicontinuous electron/ion conductive structures (Fig. 1b). The in-situ prepared Fe-PAA hydrogels on the skeleton surface of PPy aerogels serve as a reservoir providing sufficient free electrolytic ions ensuring the formation of bicontinuous conductive paths among the PAHH (Fig. 1c).

Traditional solution-processed polymerization of pyrrole always results in production of PPy in the powder form with nanoparticle-aggregated structures (Fig. S1). Surprisingly, PPy aerogels with 3D interconnected frameworks were elaborately prepared by interfacial polymerization without involving any extra agents. Ex-situ SEM observations of the intermediates at different reaction stages indicate the formation mechanism of the 3D interconnected PPy aerogels. At the early stage of interfacial polymerization, numerous isolated and loose PPy nanoparticles with sizes of several ten nanometers are observed in the corresponding sample of PPy1 with a polymerization time of 1 h (Fig. 2a, b). After 24 h of polymerization, compact microstructures consisting of inhomogeneous PPy nanoparticles with sizes ranging from several ten to a hundred nanometers begin to appear in the corresponding sample of PPy2 (Fig. 2c, d). With the further prolongation of

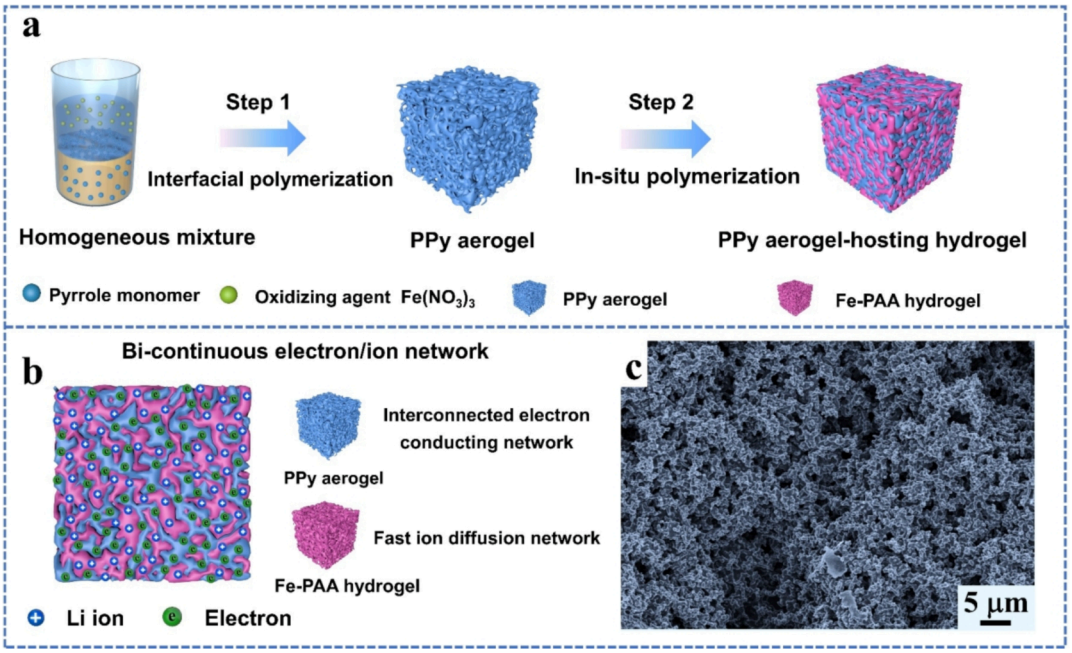

Fig. 1. Fabrication and schematic of the host–guest PAHH. (a) Schematic illustration of the preparation procedure of the PAHH. (b) Schematic illustration of PAHH with bicontinuous electron/ion-conducting networks, where PPy aerogel host and Fe-PAA hydrogel provide the 3D electron-conducting pathway and the ion reservoirs of 3D ion-conducting pathway, respectively. (c) SEM image of PAHH with 3D interconnected structures.

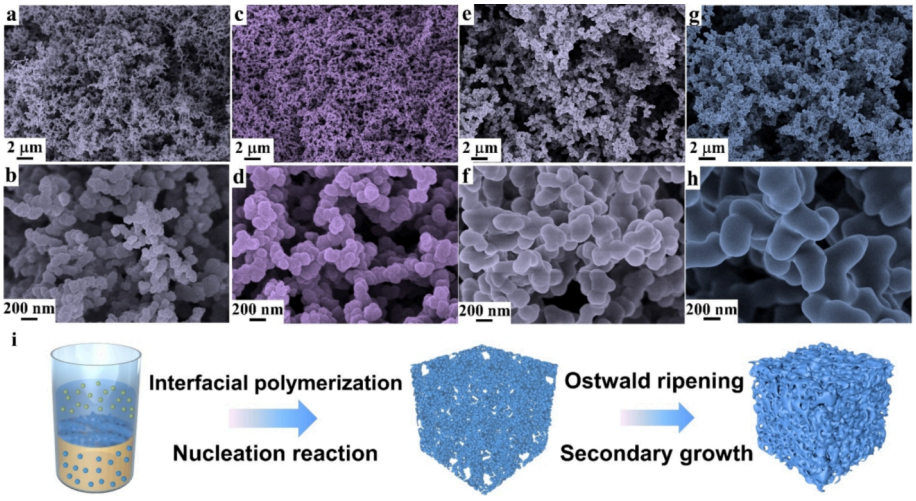

Fig. 2. Formation mechanism of PPy aerogels during the interfacial polymerization. Ex-situ SEM observations of (a, b) PPy1, (c, d) PPy2, (e, f) PPy3 and (g, h) PPy4 prepared by interfacial polymerization for 1, 24, 120 and 240 h, respectively. (i) Schematic of the formation mechanism of PPy aerogels in nucleation and Ostwald-ripening growth process during interfacial polymerization.

polymerization time, these inhomogeneous nanoparticles begin to grow to fuse, thus forming 3D interconnected and robust skeletons, as observed in PPy3 (Fig. 2e, f) and PPy4 (Fig. 2g, h).

Fig. 2i indicates the formation mechanism of 3D-interconnected PPy aerogels. The PPy might experience nucleation and secondary growths during interfacial polymerization.[39,40] The interfacial polymerization initially occurs at the interface of organic (i.e. pyrrole) and aqueous phases (i.e. mixed isopropyl alcohol, water and oxidants) (Fig. S2). Besides, the deficient oxidants strikingly suppress nucleation reactions of pyrrole monomers, resulting in the reduction of the polymerization rate and the number of primary nanoparticles among the incipient network, when compared with traditional in-situ polymerization in aqueous solution. During the nucleation stage, the already generated PPy oligomers separated from the biphasic interface of the mixed solution form small spherical nanoparticles (PPy1). As the polymerization further proceeds, the unreacted pyrrole monomers tend to be transferred and oxidatively coupled onto the surface of primary spherical PPy nanoparticles for secondary growths, thus making the original small nanoparticles grow into large interconnected PPy nanoparticles (PPy2). Furthermore, the relatively small PPy nanoparticles that possess low surface energy tend to ablate and fuse into large ones or clusters during the secondary growth stage (PPy3), according to the Ostwald ripening principle to minimize the total free energy. Finally, the PPy clusters are connected through the π-π interactions, forming a highly 3D–interconnected aerogel framework (PPy4) upon the secondary growth.

The prepared PPy aerogels demonstrate an impressive mechanical performance that could withstand compressions up to a 60% strain. The PPy aerogels also exhibit an improved compression strength with the

increment of polymerization time (Fig. S3a) because of the formation of the uniform polymeric skeleton during the slow secondary growth. The aerogel skeleton with interconnected PPy clusters provides high contacting joints, thus achieving sufficient energy dissipations during the loading–unloading cycles. The efficient energy dissipation is confirmed by the significant hysteresis loop and the energy loss coefficient is calculated during the compression (Fig. S3b). The PPy3 exhibits the smallest plastic deformation upon the loading–unloading cycles, indicating the highest elasticity among the series of PPy samples. The fabricated PPy aerogels also possess impressive water absorption/desorption capabilities during the loading–unloading cycles (Fig. S4), owing to the strong capillary effects from the 3D-interconnected structures.

The unique 3D continuous porous structure, excellent water absorption capacity and high elasticity make the PPy aerogels an ideal host candidate for preparing the PAHH electrodes via subsequent in-situ polymerization. The interfacial interaction between the PPy aerogel and Fe^{3+}PAA hydrogel is further investigated by Fourier transform infrared (FTIR) spectra (Fig. 3a). The FTIR spectrum of PPy shows absorption peaks at 1620 and 1045 cm^{-1}, corresponding to the in-ring stretching of C═C bonds and in-plane deformation of N—H bonds in pyrrole rings [41,42], respectively. The characteristic stretching frequencies include the O—H stretching at 3424 cm^{-1}, carbonyl stretching (C═O) at 1697 cm^{-1}, CH_2 scissoring at 1450 cm^{-1}, and C—O stretching vibration at 1230 cm^{-1}, which are typical absorption peaks of Fe-PAA [43]. By comparing the FTIR spectra of PPy, Fe-PAA and PAHH, the presence of PPy and Fe-PAA in the PAHH electrode is confirmed. This result further illustrates the infiltration of Fe-PAA hydrogels within the porous structure of PPy aerogels. Another peak at 1407 cm^{-1} comes from the symmetric stretching of carboxylate ions (COO$^-$) [44]. This is ascribed to the coordination of Fe^{3+} ions with PAA chains by the protonation of carboxyl groups. The abundant hydrophilic –COOH groups among the PAHH are beneficial for trapping water through hydrogen bonds as well as the dissolved electrolyte ions ($LiNO_3$), thereby enhancing the ionic conductivity. Besides, it is also observed that those peaks at 1697 cm^{-1} (C═O stretching vibration) and 1045 cm^{-1} (N—H stretching vibration) shift to relatively high wavenumbers in the FTIR spectrum of PAHH, suggesting the formation of the C═O···H—N hydrogen bonds between the Fe-PAA and PPy chains.

The weight content of PPy among the freeze-dried PAHH according to thermogravimetry analysis (TGA) results is determined as 53 wt% (Fig. S5), which makes it a promising electrode candidate with high loading of active materials. The as-fabricated PAHH maintains a typical 3D porous structure with abundant interconnected pore sizes ranging from one to several micrometers (Fig. 3b, c). Such interconnected porous structure provides both large open channels between the adjacent skeletons and nanoscaled porosities within the skeleton backbone, which is quite beneficial for achieving efficient electron transport and ion diffusion. Besides, the skeletons of PAHH are smoother than that of PPy aerogels, which is ascribed to the uniform wrapping of a slightly wrinkled PAA hydrogel layer around the PPy framework (Fig. S6). The homogenous Fe-PAA hydrogel layer overcomes the relatively rigid nature of PPy aerogels and endows the PAHH electrodes with improved elasticity. The homogeneous layer of Fe-PAA hydrogels also achieves an enlarged interface between the electrode and electrolyte with enabled ion migrations, thus benefiting the improvement of electrochemical performance.

Desirable mechanical properties are important for the host–guest electrodes in their practical applications. The as-obtained PAHH exhibits impressive elasticity (Movie S1) and compression deformation-tolerant

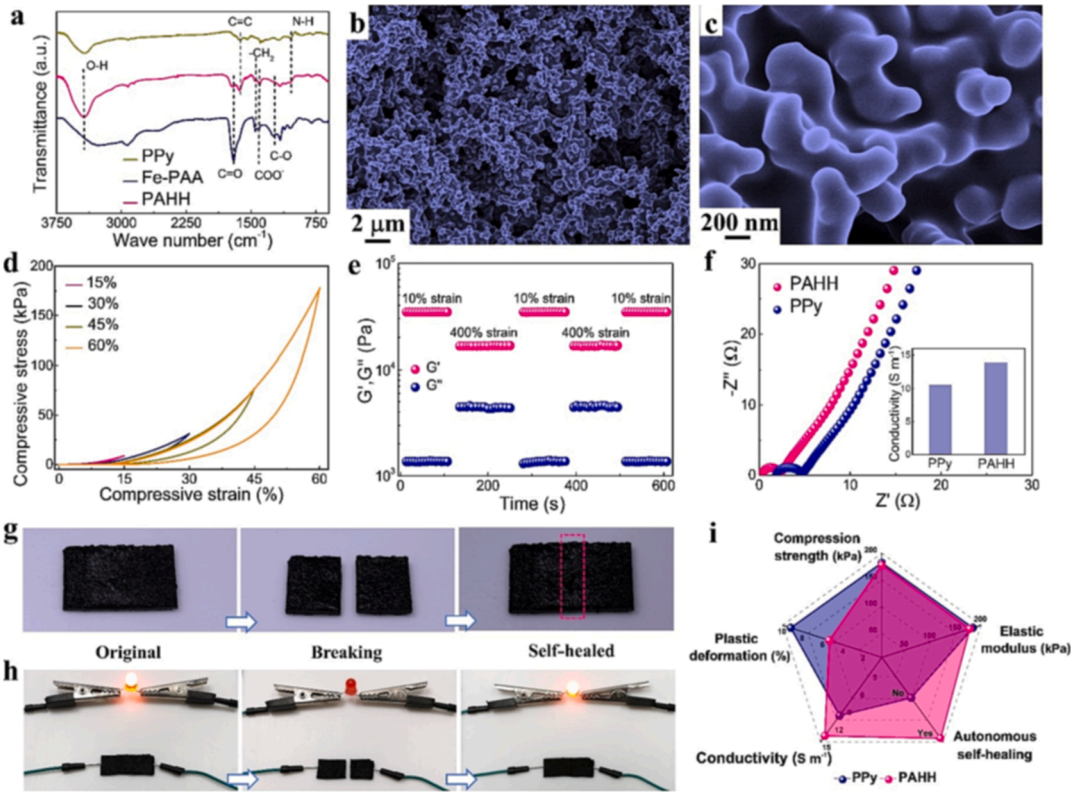

Fig. 3. Structure, mechanical and electrical properties of host–guest PAHH. (a) FTIR spectra of freeze-dried PPy, Fe-PAA and PAHH. (b, c) SEM images of freeze-dried PAHH at low and high magnifications, respectively. (d) Stress–strain curves of PAHH at compressive strains of 15 %, 30 %, 45 % and 60 %, respectively. (e) G′ and G″ of PAHH under strain sweep measurements with alternating step strains of 10 % and 400 % at an angular frequency of 1 rad s^{-1}. (f) EIS spectra of PPy and PAHH. An inset demonstrating the conductivity of PPy and PAHH. (g) Photographs showing PAHH in its original, cut and self-healed states. (h) Photographs showing PAHH as a conducting wire in a circuit for lightening a bulb during the cutting/self–healing process. (i) Comparison between the PAHH and PPy in terms of compression strength, elastic modulus, plastic deformation, conductivity and self-healability.

ability (Fig. S7), which is capable of holding its 1000-fold weight and recovering to the original shape upon unloading. Hysteresis behaviors of PAHH are observed during the loading–unloading process (Fig. 3d). The areas of hysteresis loops in the loading–unloading curves give the dissipated energy [45,46]. The hysteresis loops become remarkable with the increment of compressive strains. The dissipated energy is negligible at a small compressive strain of 15% (0.06 kJ m^{-3}) but steadily increases to 12.16 kJ m^{-3} under a compression strain of 60% (Fig. S8). The remarkable energy dissipation capability is ascribed to the deformation of hierarchical pore structures and the destruction of non-covalent interactions (i.e. π-π interactions, hydrogen bonds, coordination) among the PAHH. We further carried out the loading/unloading tests of PAHH at a compression strain of 40% to evaluate its self-recovery performance (Fig. S9). It is observed that the PAHH possesses an excellent self-recovery ability and the dissipated energy of PAHH increases with the rest time (Fig. S9a). We applied the ratio of the dissipated energy (W_{2and}/W_{1st}) that was performed in two successive compressing-releasing measurements as the recovery efficiency and found that the recovery efficiency of PAHH increased with the prolongation of rest time before reloading (Fig. S9b). The recovery efficiency of PAHH is more than 80% only after relaxing for 5 min, indicating the remarkable self-recovery performance of the PAHH. The impressive self-recovery capability of PAHH also indicates its favorable anti-fatigue performance. The anti-fatigue properties of PAHH were evaluated by carrying out multiple loading/unloading tests without any pauses between two cycles (Fig. S10). Upon 100 compression/recovery cycles at a 40% strain, the compression strength of PAHH maintains at 100% of its original value, indicating its remarkable structure integrity.

The viscoelastic properties of Fe-PAA and PAHH electrodes were evaluated by performing the frequency sweep measurements at a 1% strain, and the storage modulus (G′) and loss modulus (G″) of Fe-PAA and PAHH are depicted in Fig. S11. Both the two samples exhibit wide linear viscoelastic regions during the dynamic frequency sweep experiments. The value of G′ is higher than that of G″ in both samples, confirming their gel states [47]. Single ferric ion theoretically interacts with three carboxyl groups through electrostatic interactions, which serve as a dynamic crosslinker to construct uniform Fe-PAA networks with elastic behaviors. In addition, the G′ values of PAHH are significantly higher than that of Fe-PAA, verifying efficient mechanical reinforcements from the host–guest structure of hybrid electrodes. Cyclic step strain measurements were employed to characterize the self-healing performance of PAHH. The G′ and G″ values of PAHH under the continuous strain sweep measurements with an alternating step strain of 10% and 400% are demonstrated in Fig. 3e. Upon loading of 10% strain, the G′ and G″ values of PAHH are observed as 34.6 and 1.6 kPa, respectively, whereas the following 400% strain destroys the hydrogel network with a sudden decrease of G′ (to 16.5 kPa) and increase of G″ (to 4.7 kPa). With a continuous 10% strain step, the PAHH is recovered rapidly with a 100% healing efficiency and this process could be repeated several times without any loss in the dynamic mechanical properties. These results prove the excellent self-healing property of PAHH and the fast recovery of its network after damages. The reversible dissociation/association of hydrogen bonds between the PPy and Fe-PAA as well as the complexation inside the Fe-PAA guest are spontaneously accountable for the efficient energy dissipation and fast self-healing ability [48,49].

Owing to the formation of the PAHH with bi-continuous electron/ion networks, the conductivity of PAHH is from the two factors below: the electrical conductivity from conjugated PPy and the ionic conductivity from Fe-PAA hydrogel. By contrast, the conductivity of PPy aerogel host and PAHH was evaluated by the electrochemical impedance measurements and summarized in Fig. 3f. In the absence of Fe-PAA hydrogel, the conductivity of PPy aerogel host is measured as 10.5 S m^{-1}, which is solely contributed by electronic transports in the conjugated PPy skeleton. This value is much higher than most conducting polymer-based hydrogels in literature [18,50,51], implying the formation of efficient electron transports along with the 3D continuous PPy framework. The conductivity of PAHH is notably enhanced to 14.0 S m^{-1}, suggesting the formation of efficient ion-conducting pathways within the hybrid electrodes. Even under a compressive strain of 50%, the PAHH retains high conductivity of 12.8 S m^{-1} (Fig. S13), demonstrating its robust structural integrity.

To further demonstrate the advantages of the micro-structuring approach for preparing the hybrid electrodes, we demonstrate the self-healing ability and the conductivity recovery of PAHH samples undergoing external damage of cutting (Fig. 3g, 3 h). According to the observations of optical microscopy, the PAHH undergoes rapid self-healing processes after being cut into pieces, which is attributed to the fast reconstruction of hydrogen bonds and the efficient complexation of Fe^{3+} with PAA chains (Fig. 3g). The use of PAHH samples as a conducting wire in a circuit to light up a bulb (operating voltage: 3.0 V) confirms that the PAHH possesses an excellent conductivity (Fig. 3h). Surprisingly, the PAHH recover its original conductivity instantaneously after the cutting-healing process (Movie S2). The PAHH shows an extraordinary mechanical versatility in terms of high compression strength, high elastic modulus, large conductivity, small plastic deformation and autonomous healability (Fig. 3i). Compared with the PPy aerogel host, the hybrid electrode maintains high strength, and high elastic modulus, together with improved elasticity and conductivity. It is well known that the mechanical strength and elastic modulus usually decrease with the improvement of elasticity and self-healing efficiency [52]. It is difficult to realize electronically conductive hybrid hydrogels with conjugated polymer structures to simultaneously achieve excellent elasticity, conductivity and self-healing efficiency. Therefore, the PAHH electrodes with the combination of 3D-interconnected conducting frameworks and dynamically crosslinked networks take a step forward in the structural optimization of mechanical properties and self-healing efficiency of intrinsically elastic conducting polymer-based electrodes.

Electrochemical properties of the as-assembled all-solid-state supercapacitor (ASC) devices were first evaluated by the cyclic voltammetry (CV) and galvanostatic charge–discharge (GCD) curves in a two-electrode system. The CV curves of the ASC devices present a quasi-rectangular shape and mirror-image symmetry at a scan rate from 5 to 50 mV s^{-1} (Fig. 4a), revealing its high capacitive behavior. Upon increasing the scan rate to 100 mV s^{-1}, the CV curve deviates from the rectangular shape as a result of the diffusion limitation and large transfer resistance at a high scan rate. Meanwhile, the GCD curves of the ASC devices display a symmetrical triangle shape, indicating their outstanding capacitive behavior and fast charge–discharge ability (Fig. 4b). The specific capacitances of the ASC devices at various current densities are calculated from the GCD curves (Fig. 4c). The ASC device with 1-mm-thick electrodes reaches high gravimetric and areal capacitances of 203 F g^{-1} and 2033 mF cm^{-2}, respectively, at a current density of 2 mA cm^{-2}, which are much higher than those of flexible supercapacitors with conducting polymer hydrogel-based electrodes in literature (Table S1) [21,53–59]. Besides, the ASC device remains as high as 147.2 F g^{-1} and 1472 mF cm^{-2} at a current density of 50 mA cm^{-2}. The capacitance retention of ASC reached 72.4% under a 25-fold current density, which reveals good rate capabilities. Furthermore, the ASC devices with various mass loading of PPy are fabricated by changing the thickness of electrodes and their electrochemical performances are also investigated. The gravimetric capacitance of the device is well maintained with a slight decrease, while its areal capacitance reaches 6900 mF cm^{-2} with ultra-high PPy mass loadings of 40 mg cm^{-2} and 4-mm-thick electrodes (Fig. 4d). The areal capacitance of PAHH device was found to increase linearly with the thickness. This result indicated that the capacitance did not seriously deteriorate as the electrode thickness increased. In other words, the areal capacitance of the PAHH device could be enhanced by increasing the thickness of the electrode without sacrificing the energy-storage capacity of the material. The thickness-independent feature showed that the electronic and ionic transport within the thick PAHH was fast. For better comparison, the capacitances

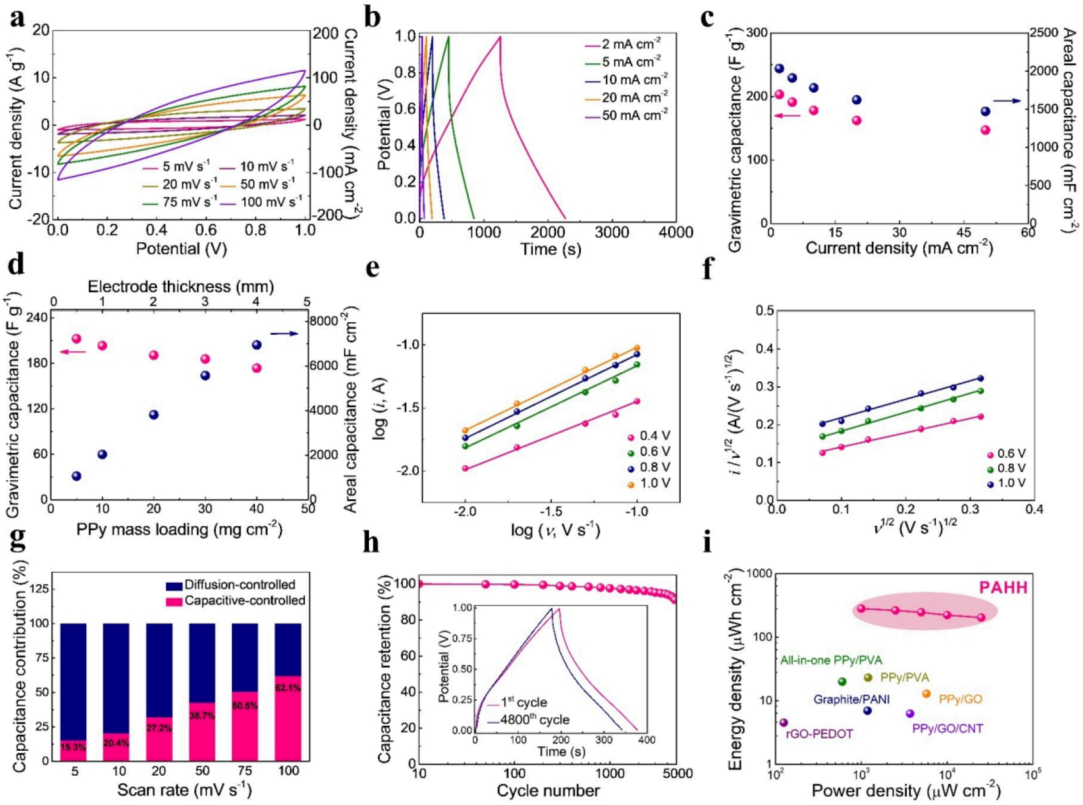

Fig. 4. Energy storage performance of PAHH in an ASC device. (a) CV curves of ASC devices at scan rates from 5 to 100 mV s^{-1}. (b) GCD curves of ASC devices at various current densities. (c) Gravimetric and areal capacitances of ASC devices at various current densities. (d) Gravimetric and areal capacitances of ASC devices with various PPy mass loadings at a current density of 2 mA cm^{-2}. (e) Plots of log(*i*) response against log(*v*) at various voltages. (f) Linear relationship between $i/v^{1/2}$ and $v^{1/2}$. (g) Quantification of ASC devices with capacitive- and diffusion-controlled capacitance contributions with the increasing scan rates. (h) Cycling performance of ASC device at a current density of 10 mA cm^{-2}. Inset showing GCD curves of the first and last cycles. (i) Ragone plots of ASC devices in comparison to supercapacitor devices based on 3D conducting polymer-based electrodes in literature.

of PPy nanoparticle electrodes with different thicknesses were also provided in Fig. S13. The PPy nanoparticle electrodes exhibited severely deteriorated specific gravimetric capacitance as the electrode thickness increased. Besides, the areal capacitance of supercapacitor with PPy nanoparticle electrodes almost stayed the same when the electrode thickness increased from 3 to 4 mm, indicating the severely deteriorated capacitance induced by the sluggish electronic and ionic transport within the thick PPy nanoparticle electrodes. The remarkably high capacitance and good rate performance are ascribed to the following factors. First, the continuous conducting path of the PPy aerogel host acts as a 3D-interconnected framework facilitating efficient electron transport. Second, the low tortuous PAHH with enlarged electrode/electrolyte interfaces promotes ion diffusion, helping accommodate strains resulting from volume changes of electrodes during the electrochemical reactions.

The outstanding electrochemical performance of the ASC devices was further evaluated through the Trasatti analysis and Dunn's methods to quantify the charge storage kinetics. According to the Trasatti analysis method, the stored charge (q) includes the ion-accessible outer surface (q_o) and inner surface (q_i) during the charging process. The dependence of q on $v^{-1/2}$ and 1/q on $v^{1/2}$ is shown in Figures S14 and S15. As a consequence, the corresponding outer charge (q_o) and total charge (q_T) are calculated as 2.67 and 14.88 C cm^{-2}, respectively. The practical charge storage is 13.03 C cm^{-2} at a high sweep rate of 75 mV s^{-1}, which accounts for 87.5 % of the total charge, indicating a high electrochemical utilization ratio of the ASC devices during the charge–discharge process. We could conclude that most of the electrode surfaces were fully accessible to electrolytic ions during the electrochemical reaction, which is ascribed to enhanced ion diffusion kinetics induced by the formation of an integrated host–guest structure. To better understand the charge storage and ion transportation mechanism of the ASC devices, Dunn's method and corresponding equations (Eqs. (S9), (S10)) were used to discuss the contributions of diffusion- and capacitive-controlled capacitances of the total storage charges. As shown in Fig. 4e and S16, the plots of log *i* versus log *v* nearly comply with a linear relationship, and the fitting results display that a series of *b*-value is less than 0.7, which represents a high diffusion-controlled contribution for the device. At the low potential, the calculated *b*-value significantly trends toward 0.5, indicating that the corresponding current is dominated by the pseudocapacitance capacitance contributions from the proton bulk transport process, which plays an indispensable role during the charge-storage process. Based on the calculated fast-kinetic process (k_1) and slow-kinetic process (k_2) values at the different voltages (Fig. 4f), the separated capacitive-controlled (fast-kinetic process) and diffusion-controlled (slow-kinetic process) contributions of the total stored charges of the ASC devices are presented in Fig. 4g. With an increase in the scan rates, the fast capacitive contributions of the devices increase from 15.3% at 5 mV s^{-1} to 62.1% at 100 mV s^{-1}. The relatively high capacitive contribution is ascribed to the short ion diffusion length and the rapid electron transfer provided by the bicontinuous electron/ion-conducting networks, which are also the reason for the achievements of rapid charge–discharge performances at high scan rates.

The ASC devices also present excellent cycling stability with more than 95% and 90% of retentions after 3000 and 4800 cycles, respectively (Fig. 4h). The desirable high cycling stability of PAHH is attributed to the formation of the 3D interconnected PPy framework and the integrated electrode/electrolyte structure. First, the PAHH with the 3D

interconnected PPy framework provides an efficient charge transport and helps accommodate strains resulting from volume changes during the electrochemical reaction. Second, the PAHH with the integration of electron/ion-conducting phases enlarges the interface between the electrode and electrolyte, thereby shortening the ion diffusion pathway and enabling enhanced ion diffusion kinetics for redox reactions. At last, the tough Fe-PAA hydrogel reinforces the structural integrity of PAHH throughout long-term cycling and helps maintain the electrochemical stability of the 3D electrodes. These unique structural characteristics simultaneously make contributions to optimizing the as-fabricated ASC devices with largely enhanced energy storage and cycling stability. The Ragone plots of the ASC devices are illustrated in Fig. 4i. The ASC device exhibits a high energy density of 204.2 μWh cm^{-2} at a power density of 25000 μW cm^{-2}, which is among the top of the state-of-the-art flexible supercapacitors with conducting polymer hydrogels as the electrode [53–58]. Detailed comparisons are listed in Table S1.

As demonstrated above, the dynamically reversible interactions between PPy and Fe-PAA as well as the complexations between PAA and Fe^{3+} ions endow the PAHH with ideal compressibility and self-healing ability. More importantly, the PAHH is capable of maintaining its original 3D conductive network, mechanical property, viscoelasticity and charge transport capability after multiple compression or cutting/self-healing processes, which is especially promising for the assembly of compressible and self-healing supercapacitors. The PAHH exhibits high retention of its original capacitance under various compression strains, as demonstrated by their almost overlapped CV curves in Fig. 5a. Remarkably, the PAHH-based ASC device maintains nearly 90% of its original capacitance under a 60% compression, calculated from the GCD curves (Fig. S17). The equivalent series resistance (*ESR*) and *RC* time constants of the device, which are obtained from the Nyquist and Bode plots, respectively (Fig. 5b, S18), almost stay the same under various compression strains, implying the stable electron/ion transport of PAHH. After a series of cutting/self-healing cycles, slightly decreased CV curves area (Fig. 5c) and discharge time of GCD curves (Fig. S19) are respectively observed. As estimated from the GCD curves in Fig. S16, the self-healing efficiency of the device is more than 80% after five cycles of the cutting/self-healing processes, suggesting that the self-healing ability and the capability to automatically restore its original capacitive performance of PAHH each time from serious external damages. Slightly increased *ESR* and *RC* time constants (obtained from Fig. 5d and Fig. S20) are observed with more repeated cutting/self-healing cycles, implying the marginally deteriorated electron/ion transport and slightly decreased capacitance performance. Besides, the ion diffusion resistance (σ) of PAHH ASC after different cutting/self-healing cycles were compared (Fig. S21). The values of σ were extracted from the slopes of the linear fitting lines of the real part of impedance (Z′) versus the reciprocal of the square root of frequency ($\omega^{-0.5}$). The ion diffusion resistance increased with the increment of cutting/self-healing cycles. After 5 cutting/self-healing cycles, the σ value reached 8.96 Ω $s^{-0.5}$, which is twice the initial value (4.12 Ω $s^{-0.5}$). This result indicates the sluggish ion diffusion kinetics of PAHH ASC after repeatedly cutting/self-healing cycles. Therefore, the deteriorated electron transportation and the sluggish ion diffusion kinetics of PAHH lead to capacitance degradation after 5 cutting/self-healing cycles.

Generally, the total energy stored in a single ASC device is not always high enough to meet the practical applications. Accordingly, the assembly of several individual devices in series is an effective way to obtain an integrated energy storage device with specifically tailored output voltages. Herein, the assembly of two and three series-connected PAHH-based ASC devices was achieved. The device in series with an assembly of two and three independent ASC devices shows an increasing output potential of 2.0 and 3.0 V, respectively (Fig. 5e). The remarkable electrochemical performance of the series-connected ASC devices is also confirmed by GCD tests in Fig. 5f. The series-connected ASC devices not only maintain the stable output capacitance that was proved by similar discharge time but also obtain the high voltage window. As a demonstration, an integrated energy storage unit consisting of three series-connected ASC devices is assembled to power external circuitry. As a proof-of-concept, the resultant integrated energy storage unit is powerful to light up a red light-emitting diode (LED) bulb after being fully charged (Fig. 5g). More importantly, the integrated energy storage unit also works well when being sustained in large compression deformation. Furthermore, when one supercapacitor of the integrated unit was cut off, the integrated energy storage unit could restore its initial capacitance after being simply self-healed, suggesting the excellent self-healing characteristic of the integrated devices (Fig. 5h).

To further understand the influences of the electrode/electrolyte integration and the bicontinuous network structure of the PAHH on the corresponding electrochemical properties, the electrochemical performance of ASC devices based on PAHH and PPy was fully investigated. As illustrated in Fig. 6a, the PAHH-based ASC device exhibits largely enhanced specific capacitances and improved rate capabilities

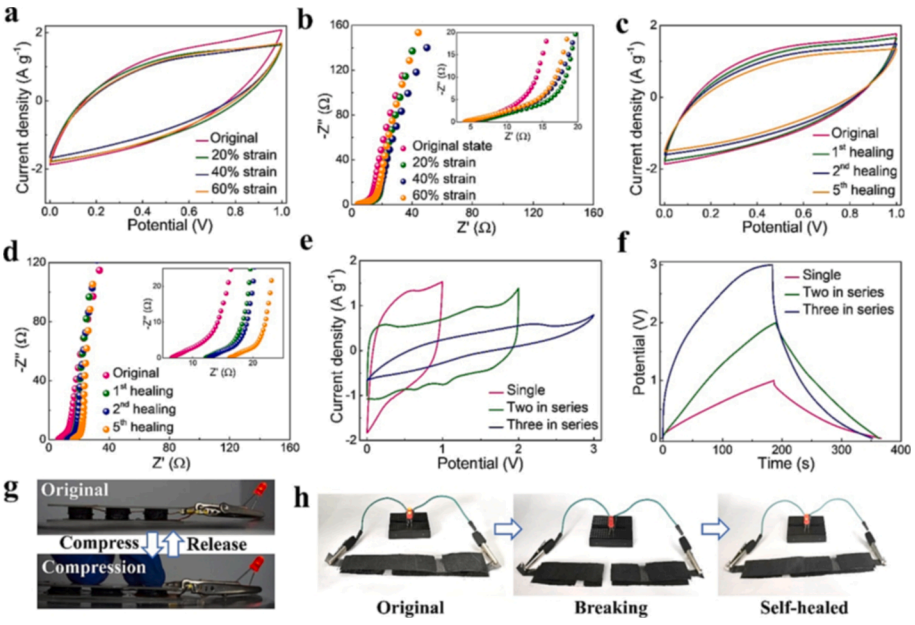

Fig. 5. Deformation-tolerant performance of ASC devices with the PAHH. (a) CV curves of ASC devices under various compressive strains at a scan rate of 10 mV s^{-1}. (b) Nyquist plots of ASC devices under various compressive strains. Inset showing the high-frequency region. (c) CV curves and (d) Nyquist plots of ASC devices before and after multiple cutting/self-healing cycles at a scan rate of 10 mV s^{-1}. Inset of (d) showing the high-frequency region. CV curves and GCD curves of one, two and three ASC devices connected in series at (e) scan rate of 10 mV s^{-1} and (f) current density of 10 mA cm^{-2}, respectively. (g) Photographs showing an integrated device with three series-connected ASC devices lightening up a bulb at original and compressive states, respectively. (h) Demonstrations of the cutting/self-healing process of the integrated device.

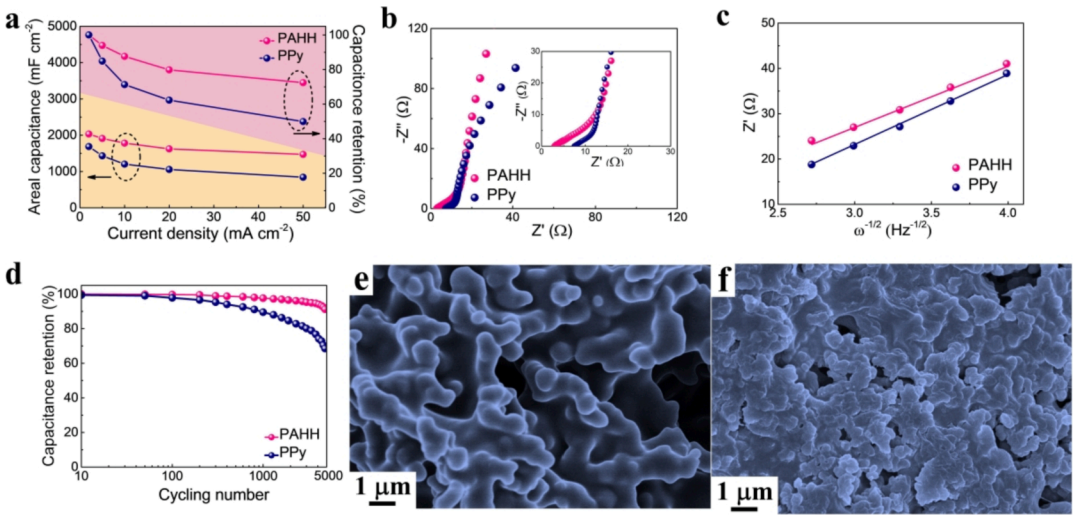

Fig. 6. Contribution of microstructure on electrochemical properties. (a) Capacitances of ASC devices based on PAHH and PPy at various current densities. (b) Nyquist plots of ASC devices based on PAHH and PPy. Inset showing the high-frequency region. (c) Linear fittings showing the relationship between Z' and $\omega^{-1/2}$ of ASC devices based on PAHH and PPy in low-frequency region. (d) Cycling stability of ASC devices based on PAHH and PPy. (e-f) SEM images of PAHH and PPy electrodes after long-term cycling.

compared with those of PPy-based ASC devices, especially at a large current density. We suggest that the largely improved capacitance and rate performance of the ASC devices are ascribed to the formation of the unique design of bicontinuous electrode/electrolyte integration, which gives rise to the enlarged interfaces between the electrode and electrolyte with enhanced ion diffusion kinetics for redox reactions. The Nyquist plots and Bode plots are provided to investigate the ion diffusion kinetics of both supercapacitors. The Nyquist plots of ASC devices with the PAHH and PPy electrodes show the respective high-, mid-, and low-frequency regions (Fig. 6b), which correspond to the electro-transfer limited process, the diffusion-limited process and the capacitive behavior, respectively [18]. The high-frequency region is a reflection of the electrical conductivity of electrodes and the redox charge-transfer reaction at the electrode–electrolyte interface. The conductivity of supercapacitor electrodes is measured in terms of the equivalent series resistance (*ESR*), which is obtained from the first intercept of the Nyquist plots on the real impedance axis. The *ESR* comprises the intrinsic resistance of an electrode, the contact resistance with the current collector, and the electrolyte resistance. The PAHH-based ASC device exhibits a smaller *ESR* than that of the PPy-based ASC device. In the mid-frequency region, the charge-transfer reaction at the electrode–electrolyte interface is always expressed as a semicircle [59]. Distorted semicircular arcs are observed from the PAHH and PPy-based ASC devices, respectively, which are ascribed to the overlapping of high-frequency redox reactions and mid-frequency reactions induced by the formation of 3D-interconnected PPy frameworks [18]. The nearly straight line at the low-frequency region demonstrates excellent capacitive behaviors of the devices without significant diffusion limitations. The Bode plot explains that the total impedance decreases with the increment in frequency (Fig. S22). The characteristic frequency f_o at a phase angle of -45° or its corresponding relaxation time, also called the *RC* time constant, marks the point where the resistive and capacitive impedances are equal [60]. The PAHH and PPy exhibit a f_o of 0.215 and 0.121 Hz, respectively, corresponding to the *RC* time constant of 4.65 and 8.26 s, respectively. The fast frequency response of PAHH indicates enhanced ion transports within hybrid electrodes with the electrode/electrolyte integration design. The Randles plot demonstrates the relationship between Z' and $\omega(\omega\ 2\pi^*f)$ in the low-frequency region (Fig. 6c) and the slope of the linear fitting represents the Warburg factor [61]. The PAHH-based ASC device presents a low Warburg factor, demonstrating enhanced ion diffusion kinetics compared with that of the PPy-based ASC.

The PAHH-based ASC devices exhibit largely improved cycling stability compared with that of devices based on PPy aerogels (Fig. 6d). The unique bicontinuous structure of the PAHH electrode with the integrity of tough Fe-PAA hydrogel reinforcing 3D PPy aerogel host is critical for its outstanding cycling stability. This hypothesis is also proved by the SEM images of PAHH and PPy electrodes after long-term cycling. A well-defined bicontinuous configuration of PAHH is well maintained after long-term charge/discharge cycles (Fig. 6e), indicating its excellent structural integrity. By contrast, the porous and interconnected framework of PPy aerogels is almost destroyed owing to serious volume expansions of the electrode and the largely blocked gel electrolyte after long-term cycling (Fig. 6f). These results imply that the PAHH with bicontinuous electrode/electrolyte structures improves both the rate and cycling performance by facilitating ionic transport and improving the structural integrity, respectively. These findings are of significant importance for fabricating novel hybrid electrodes for high-performance energy storage devices with largely improved rate and cycling performance.

4. Conclusion

In summary, we have established a new strategy for creating host–guest hydrogel electrodes with bicontinuous conductive structures. The PPy aerogel-hosting hydrogel electrodes are developed by triggering in-situ polymerization of Fe-PAA hydrogels constrained to the skeleton surface of 3D interconnected PPy aerogels. Taking the advantage of the reversible nature of noncovalent cross-linking of hydrogen bonds and metal coordinations, the resultant PAHH electrodes demonstrate superelasticity, high conductivity, excellent capacitance performance and intrinsic self-healability. The bicontinuous electron/ion conductive structures within the PAHH not only provide remarkable conductivity but also endow enhanced redox reactions and ion transport kinetics. The PAHH-based ASC devices with an integrated electrode/electrolyte interface simultaneously display an ultra-high capacitance of 6900 mF cm^{-2} (PPy mass loading to 40 mg cm^{-2}), excellent rate performance (80% retention at a 25-fold current density) and high cycling stability (95% retention after 3000 cycles). Furthermore, the promising structural design of PAHH with the unique bicontinuous structures endows flexible supercapacitors with steady capacitance retentions under mechanical deformations and even physical damages. This study therefore presents a novel and efficient strategy to construct conducting polymer hydrogels with bicontinuous electron/ion-conducting paths for smart

energy storage in next-generation electrochemical/electronic systems.

Declaration of Competing Interest

The authors declare that they have no known competing financial interests or personal relationships that could have appeared to influence the work reported in this paper.

Data availability

Data will be made available on request.

Acknowledgments

The authors are grateful for the support from the National Natural Science Foundation of China (21875033, 52003107, 52122303), Shanghai Scientific and Technological Innovation Project (22520714500), the China Postdoctoral Science Foundation (2021M691266), and the Jiangsu Province Postdoctoral Science Foundation (2021K168B).

Appendix A. Supplementary data

Supplementary data to this article can be found online at https://doi.org/10.1016/j.cej.2022.139223.

References

[1] W. Zhang, P. Feng, J. Chen, Z.M. Sun, B.X. Zhao, Electrically conductive hydrogels for flexible energy storage systems, Prog. Polym. Sci. 88 (2019) 220–240.
[2] M. Wang, Y. Feng, Y. Zhang, S. Li, M. Wu, L. Xue, J. Zhao, W. Zhang, M. Ge, Y. Lai, J. Mi, Ion regulation of hollow nickel cobalt layered double hydroxide nanocages derived from ZIF-67 for high-performance supercapacitors, Appl. Surf. Sci. 596 (2022), 153582.
[3] H. Wang, B. Zhu, W. Jiang, Y. Yang, W.R. Leow, H. Wang, X. Chen, A mechanically and electrically self-healing supercapacitor, Adv. Mater. 26 (2014) 3638–3643.
[4] Q. Yin, L. Chen, Y. Chen, F. Zhan, A high-performance flexible aqueous silver-Zinc rechargeable battery based on AgNP/CNT-graphite paper and ZnNF-graphite paper, Compos. Commun. 26 (2021), 100728.
[5] Q. Fu, S. Hao, L. Meng, F. Xu, J. Yang, Engineering self-adhesive polyzwitterionic hydrogel electrolytes for flexible Zinc-ion hybrid capacitors with superior low-temperature adaptability, ACS Nano 15 (2021) 18469–18482.
[6] X. Huang, Q. Niu, S. Fan, Y. Zhang, Highly oriented lamellar polyaniline with short-range disorder for enhanced electrochromic performance, Chem. Eng. J. 417 (2021), 128126.
[7] L. Li, K. Wang, Z.Q. Huang, C. Zhang, T.X. Liu, Highly ordered graphene architectures by duplicating melamine sponges as a three-dimensional deformation-tolerant electrode, Nano Research 9 (2016) 2938–2949.
[8] Z.Q. Huang, L. Li, Y.F. Wang, C. Zhang, T.X. Liu, Polyaniline/graphene nanocomposites towards high-performance supercapacitors: a review, Compos. Commun. 8 (2018) 83–91.
[9] Y. Huang, M. Zhong, Y. Huang, M. Zhu, Z. Pei, Z. Wang, Q. Xue, X. Xie, C. Zhi, A self-healable and highly stretchable supercapacitor based on a dual crosslinked polyelectrolyte, Nat. Commun. 6 (2015) 10310.
[10] H. Wang, H. Yang, Y. Diao, Y. Lu, K. Chrulski, J.M. D'Arcy, Solid-state precursor impregnation for enhanced capacitance in hierarchical flexible poly(3,4-ethylenedioxythiophene) supercapacitors, ACS Nano 15 (2021) 7799–7810.
[11] N. Swain, A. Tripathy, A. Thirumurugan, B. Saravanakumar, L. Schmidt-Mende, A. Ramadoss, A brief review on stretchable, compressible, and deformable supercapacitor for smart devices, Chem. Eng. J. 446 (2022), 136876.
[12] Y.Q. Wang, Y. Ding, X.L. Guo, G.H. Yu, Conductive polymers for stretchable supercapacitors, Nano Res. 12 (2019) 1978–1987.
[13] W. Li, F. Gao, X. Wang, N. Zhang, M. Ma, Strong and robust polyaniline-based supramolecular hydrogels for flexible supercapacitors, Angew. Chem. Int. Ed. 55 (2016) 9196–9201.
[14] J. Zeng, L. Dong, W. Sha, L. Wei, X. Guo, Highly stretchable, compressible and arbitrarily deformable all-hydrogel soft supercapacitors, Chem. Eng. J. 383 (2020), 123098.
[15] J. Xu, R. Jin, X. Ren, G. Gao, A wide temperature-tolerant hydrogel electrolyte mediated by phosphoric acid towards flexible supercapacitors, Chem. Eng. J. 413 (2021), 127446.
[16] F. Zhao, J. Bae, X. Zhou, Y. Guo, G. Yu, Nanostructured functional hydrogels as an emerging platform for advanced energy technologies, Adv. Mater. 30 (2018) 1801796.
[17] T.X. Zhu, Y. Cheng, C.Y. Cao, J.J. Mao, L.Q. Li, J.Y. Huang, S.W. Gao, X.L. Dong, Z. Chen, Y.K. Lai, A semi-interpenetrating network ionic hydrogel for strain sensing with high sensitivity, large strain range, and stable cycle performance, Chem. Eng. J. 385 (2020), 123912.
[18] L. Li, Y. Zhang, H. Lu, Y. Wang, J. Xu, J. Zhu, C. Zhang, T. Liu, Cryopolymerization enables anisotropic polyaniline hybrid hydrogels with superelasticity and highly deformation-tolerant electrochemical energy storage, Nat. Commun. 11 (2020) 62.
[19] Y. Wang, M. Wang, P. Wang, W. Zhou, Z. Chen, Q. Gao, M. Shen, J. Zhu, Urea-treated wet-spun PEDOT: PSS fibers for achieving high-performance wearable supercapacitors, Compos. Commun. 27 (2021), 100885.
[20] J. Zhang, X. Fan, X. Meng, J. Zhou, M. Wang, S. Chen, Y. Cao, Y. Chen, C. W. Bielawski, J. Geng, Ice-templated large-scale preparation of two-dimensional sheets of conjugated polymers: thickness-independent flexible supercapacitance, ACS Nano 15 (2021) 8870–8882.
[21] F. Chen, Q. Chen, Q. Song, H. Lu, M.M. Ma, Strong and stretchable polypyrrole hydrogels with biphase microstructure as electrodes for substrate-free stretchable supercapacitors, Adv. Mater. Interfaces 6 (2019) 1900133.
[22] M. Hua, S. Wu, Y. Jin, Y. Zhao, B. Yao, X. He, Tough-hydrogel reinforced low-tortuosity conductive networks for stretchable and high-performance supercapacitors, Adv. Mater. 33 (2021) 2100983.
[23] M. Qiu, H. Liu, B. Tawiah, H. Jia, S. Fu, Zwitterionic triple-network hydrogel electrolyte for advanced flexible Zinc ion batteries, Compos. Commun. 28 (2021), 100942.
[24] X. Sui, H. Guo, C. Cai, Q. Li, C. Wen, X. Zhang, X. Wang, J. Yang, L. Zhang, Ionic conductive hydrogels with long-lasting antifreezing, water retention and self-regeneration abilities, Chem. Eng. J. 419 (2021), 129478.
[25] L. Pan, G. Yu, D. Zhai, H.R. Lee, W. Zhao, N. Liu, H. Wang, B.C. Tee, Y. Shi, Y. Cui, Z. Bao, Hierarchical nanostructured conducting polymer hydrogel with high electrochemical activity, Proc. Natl. Acad. Sci. U.S.A. 109 (2012) 9287–9292.
[26] Y. Wang, Y. Shi, L. Pan, Y. Ding, Y. Zhao, Y. Li, Y. Shi, G. Yu, Dopant-enabled supramolecular approach for controlled synthesis of nanostructured conductive polymer hydrogels, Nano Lett. 15 (2015) 7736–7741.
[27] Z.W. Wang, J. Chen, Y. Gong, H. Zhang, T. Xu, L. Nie, J. Fu, Ultrastretchable strain sensors and arrays with high sensitivity and linearity based on super tough conductive hydrogels, Chem. Mater. 30 (2018) 8062–8069.
[28] P. Bober, J. Pfleger, I.A. Pasti, N. Gavrilov, S.K. Filippov, D. Klepac, M. Trchova, H. Hlidkova, J. Stejskal, Carbogels: Carbonized conducting polyaniline/poly(vinyl alcohol) aerogels derived from cryogels for electrochemical capacitors, J. Mater. Chem. A 7 (2019) 1785–1796.
[29] Q. Ding, X. Xu, Y. Yue, C. Mei, C. Huang, S. Jiang, Q. Wu, J. Han, Nanocellulose-mediated electroconductive self-healing hydrogels with high strength, plasticity, viscoelasticity, stretchability, and biocompatibility toward multifunctional applications, ACS Appl. Mater. Inter. 10 (2018) 27987–28002.
[30] Y. Guo, K. Zheng, P. Wan, A flexible stretchable hydrogel electrolyte for healable all-in-one configured supercapacitors, Small 14 (2018) 1704497.
[31] Y. Shi, C. Ma, L. Peng, G. Yu, Conductive "smart" hybrid hydrogels with pnipam and nanostructured conductive polymers, Adv. Funct. Mater. 25 (2015) 1219.
[32] F. Wang, J.Y. Cheong, Q. He, G. Duan, S. He, L. Zhang, Y. Zhao, I.-D. Kim, S. Jiang, Phosphorus-doped thick carbon electrode for high-energy density and long-life supercapacitors, Chem. Eng. J. 414 (2021), 128767.
[33] J. Wang, M. Wang, N. Ren, J. Dong, Y. Li, C. Chen, High-areal-capacity thick cathode with vertically-aligned micro-channels for advanced lithium ion batteries, Energy Storage Mater. 39 (2021) 287–293.
[34] J.T. Lee, C. Jo, M. De Volder, Bicontinuous phase separation of lithium-ion battery electrodes for ultrahigh areal loading, Proc. Natl. Acad. Sci. U.S.A. 117 (2020) 21155–21161.
[35] J. Wu, Z. Ju, X. Zhang, C. Quilty, K.J. Takeuchi, D.C. Bock, A.C. Marschilok, E. S. Takeuchi, G. Yu, Ultrahigh-capacity and scalable architected battery electrodes via tortuosity modulation, ACS Nano 15 (2021) 19109–19118.
[36] Z. Xu, R. Ma, X. Wang, Ultrafast, long-life, high-loading, and wide-temperature zinc ion supercapacitors, Energy Storage Mater. 46 (2022) 233–242.
[37] B. Asbani, G. Buvat, J. Freixas, M. Huvé, D. Troadec, P. Roussel, T. Brousse, C. Lethien, Ultra-high areal capacitance and high rate capability RuO_2 thin film electrodes for 3D micro-supercapacitors, Energy Storage Mater. 42 (2021) 259–267.
[38] S.P. Li, R.Y. Xiong, Z.L. Han, R.J. He, S.W. Li, H.M. Zhou, C. Yu, S.J. Cheng, J. Xie, Unveiling low-tortuous effect on electrochemical performance toward ultrathick $LiFePO_4$ electrode with 100 mg cm^{-2} area loading, J. Power Sources 515 (2021), 230588.
[39] J. Huang, R.B. Kaner, Nanofiber formation in the chemical polymerization of aniline: A mechanistic study, Angew. Chem. Int. Ed. 43 (2004) 5817–5821.
[40] F. Zhang, J.B. Fan, S. Wang, Interfacial polymerization: From chemistry to functional materials, Angew. Chem. Int. Ed. 59 (2020) 21840–21856.
[41] Y. Shi, L.J. Pan, B.R. Liu, Y.Q. Wang, Y. Cui, Z.A. Bao, G.H. Yu, Nanostructured conductive polypyrrole hydrogels as high-performance, flexible supercapacitor electrodes, J. Mater. Chem. A 2 (2014) 6086–6091.
[42] R. Wang, Z. Tan, W. Zhong, K. Liu, M. Li, Y. Chen, W. Wang, D. Wang, Polypyrrole (PPy) attached on porous conductive sponge derived from carbonized graphene oxide coated polyurethane (PU) and its application in pressure sensor, Compos. Commun. 22 (2020), 100426.
[43] X. Zhang, Z. Pei, C. Wang, Z. Yuan, L. Wei, Y. Pan, A. Mahmood, Q. Shao, Y. Chen, Flexible Zinc-ion hybrid fiber capacitors with ultrahigh energy density and long cycling life for wearable electronics, Small 15 (2019) 1903817.
[44] L.J. Kirwan, P.D. Fawell, W. van Bronswijk, In situ FTIR-ATR examination of poly (acrylic acid) adsorbed onto hematite at low pH, Langmuir 19 (2003) 5802–5807.
[45] Y. Yang, X. Wang, F. Yang, H. Shen, D. Wu, A universal soaking strategy to convert composite hydrogels into extremely tough and rapidly recoverable double-network hydrogels, Adv. Mater. 28 (2016) 7178–7184.

[46] Y. Hu, Z.S. Du, X.L. Deng, T. Wang, Z.H. Yang, W.Y. Zhou, C.Y. Wang, Dual physically cross-linked hydrogels with high stretchability, toughness, and good self-recoverability, Macromolecules 49 (2016) 5660–5668.
[47] J.S. Chen, Q.Y. Peng, T. Thundat, H.B. Zeng, Stretchable, injectable, and self-healing conductive hydrogel enabled by multiple hydrogen bonding toward wearable electronics, Chem. Mater. 31 (2019) 4553–4563.
[48] Z.J. Wei, J. He, T. Liang, H. Oh, J. Athas, Z. Tong, C.Y. Wang, Z.H. Nie, Autonomous self-healing of poly(acrylic acid) hydrogels induced by the migration of ferric ions, Polym. Chem. 4 (2013) 4601–4605.
[49] Y. Huang, J. Liu, J.Q. Wang, M.M. Hu, F.A. Mo, G.J. Liang, C.Y. Zhi, An intrinsically self-healing nico vertical bar vertical bar zn rechargeable battery with a self-healable Ferric-ion-crosslinking sodium polyacrylate hydrogel electrolyte, Angew. Chem. Int. Ed. 57 (2018) 9810–9813.
[50] Y. Shi, C.B. Ma, L.L. Peng, G.H. Yu, Conductive “smart” hybrid hydrogels with pnipam and nanostructured conductive polymers, Adv. Funct. Mater. 25 (2015) 1219–1225.
[51] W. Li, X.P. Zeng, H. Wang, Q. Wang, Y.J. Yang, Polyaniline-poly(styrene sulfonate) conducting hydrogels reinforced by supramolecular nanofibers and used as drug carriers with electric-driven release, Eur. Polym. J. 66 (2015) 513–519.
[52] Z. Lei, P. Wu, A highly transparent and ultra-stretchable conductor with stable conductivity during large deformation, Nat. Commun. 10 (2019) 3429.
[53] B. Yao, L.Y. Yuan, X. Xiao, J. Zhang, Y.Y. Qi, J. Zhou, J. Zhou, B. Hu, W. Chen, Paper-based solid-state supercapacitors with pencil-drawing graphite/polyaniline networks hybrid electrodes, Nano Energy 2 (2013) 1071–1078.
[54] L. Zang, Q. Liu, J. Qiu, C. Yang, C. Wei, C. Liu, L. Lao, Design and fabrication of an all-solid-state polymer supercapacitor with highly mechanical flexibility based on polypyrrole hydrogel, ACS Appl. Mater. Interfaces 9 (2017) 33941–33947.
[55] H.H. Zhou, G.Y. Han, Y.M. Xiao, Y.Z. Chang, H.J. Zhai, Facile preparation of polypyrrole/graphene oxide nanocomposites with large areal capacitance using electrochemical codeposition for supercapacitors, J. Power Sources 263 (2014) 259–267.
[56] K. Sun, E. Feng, G. Zhao, H. Peng, G. Wei, Y. Lv, G. Ma, A single robust hydrogel film based integrated flexible supercapacitor, ACS Sustain. Chem. Eng. 7 (2018) 165–173.
[57] H.H. Zhou, H.J. Zhai, A highly flexible solid-state supercapacitor based on the carbon nanotube doped graphene oxide/polypyrrole composites with superior electrochemical performances, Org. Electron. 37 (2016) 197–206.
[58] B. Li, J.L. Cheng, Z.P. Wang, Y.C. Li, W. Ni, B. Wang, Highly-wrinkled reduced graphene oxide-conductive polymer fibers for flexible fiber-shaped and interdigital-designed supercapacitors, J. Power Sources 376 (2018) 117–124.
[59] K.V. Sankar, R.K. Selvan, The ternary $MnFe_2O_4$/graphene/polyaniline hybrid composite as negative electrode for supercapacitors, J. Power Sources 275 (2015) 399–407.
[60] X. Wu, Y. Xu, Y. Hu, G. Wu, H. Cheng, Q. Yu, K. Zhang, W. Chen, S. Chen, Microfluidic-spinning construction of black-phosphorus-hybrid microfibres for non-woven fabrics toward a high energy density flexible supercapacitor, Nat. Commun. 9 (2018) 4573.
[61] J. Yan, C.E. Ren, K. Maleski, C.B. Hatter, B. Anasori, P. Urbankowski, A. Sarycheva, Y. Gogotsi, Flexible MXene/graphene films for ultrafast supercapacitors with outstanding volumetric capacitance, Adv. Funct. Mater. 27 (2017) 1701264.